Chinese Chemical Letters 36 (2025) 109715

Contents lists available at ScienceDirect

Chinese Chemical Letters

journal homepage: www.elsevier.com/locate/cclet

Phase engineering and heteroatom incorporation enable defect-rich MoS_2 for long life aqueous iron-ion batteries

Xinyu Guo[1], Chang Li[1], Wenjun Deng, Yi Zhou, Yan Chen, Yushuang Xu, Rui Li*

School of Advanced Materials, Peking University Shenzhen Graduate School, Shenzhen 518055, China

ARTICLE INFO

Article history:
Received 15 January 2024
Revised 20 February 2024
Accepted 1 March 2024
Available online 6 March 2024

Keywords:
MoS_2
Controllable phase engineering
Aqueous iron-ion batteries
Fe^{2+} intercalation
Iron metal anode

ABSTRACT

Aqueous iron-ion batteries are regarded as one of the most promising candidates for grid applications owing to their low cost, high theoretical capacity, and excellent stability of iron in aqueous electrolytes. However, the slow Fe (de)insertion caused by the high polarity of Fe^{2+} makes it difficult to match suitable cathode materials. Herein, defect-rich MoS_2 with abundant 1T phase is synthesized and successfully applied in aqueous iron-ion batteries. Benefit from abundant active sites generated by the heteroatom incorporation and S vacancy, as well as the highly conductive 1T phase, it can deliver a specific capacity of 123 mAh/g at a current density of 100 mA/g, and demonstrates an impressive capacity retention of 88% after 600 cycles at 200 mA/g. This work presents a novel pathway for the advancement of cathode materials for aqueous iron-ion batteries.

The substantial energy demand in contemporary society and the limited availability of fossil fuels have engendered a profound contradiction, leading to the rapid advancement of renewable energy [1–3]. Energy storage systems play a pivotal role in this progress owing to the unsteadiness of renewable energy in the temporal distribution [4]. Despite the significant commercial success lithium-ion batteries made in portable devices and electric vehicles, their intrinsic flammability poses a challenge for further advancements in grid-scale energy storage systems [5]. Aqueous batteries exhibit significant advantages in terms of safety and cost compared to organic lithium-ion batteries, owing to their non-flammable nature and low-cost aqueous electrolyte. This renders them highly promising for large-scale energy storage applications [6].

In recent years, the majority of research in aqueous batteries has primarily focused on zinc-ion batteries, which are plagued by significant hydrogen evolution, Zn corrosion, and dendrite formation [7–11]. However, alternative metal anodes have remained largely unexplored for aqueous batteries, among which iron shows exceptional promise [12,13]. Compared to zinc-ion batteries, iron-ion batteries exhibit several advantages. Firstly, iron ranks as the fourth most abundant element in the earth's crust, surpassing zinc reserves by a significant margin (4.65 wt% of iron compared to 0.0083 wt% of zinc) [14,15]. The substantial availability of iron, coupled with well-established processing techniques, contributes to its remarkably low price of $60 per metric ton in contrast to zinc priced at $2600 [13]. Besides, the redox potential of iron (−0.44 V *vs.* standard hydrogen electrode (SHE)) is comparatively higher than that of zinc (−0.76 V *vs.* SHE), thereby ensuring enhanced stability of iron metal in aqueous electrolytes [16]. Moreover, iron metal exhibits superior gravimetric capacity (960 mAh/g) and volumetric capacity (7558 mAh/cm^3) compared to zinc metal (820 mAh/g and 5854 mAh/cm^3) [17]. In addition, iron metal is less prone to form dendrites, enhancing the safety and stability of batteries [12]. Consequently, aqueous iron-ion battery is a promising alternative to aqueous zinc-ion battery.

However, the research of aqueous iron-ion batteries based on Fe^{2+} (de)intercalation remains in its nascent stages. Due to the redox potential of Fe^{3+}/Fe^{2+} (0.77 V *vs.* SHE), it is difficult to exploit suitable cathode materials working in such a narrow voltage window (0–1.21 V *vs.* Fe^{2+}/Fe) [18]. Till now, only a few materials have been exploited for aqueous iron-ion batteries, such as Prussian blue analogue [17], $VOPO_4{\cdot}2H_2O$ [16], PA@$VOPO_4$ [19], sulfur [20], I_2 [21], polyaniline [18,22] and VO_2 [23]. However, these materials are not satisfactory in terms of capacity or cycle stability. Efforts are still required to develop cathode materials exhibiting exceptional electrochemical performance for aqueous iron-ion batteries.

MoS_2, as a classical two-dimensional transition-metal dichalcogenide, has been wildly utilized in several types of ion batteries as cathode material such as Li-ion batteries [24], Na-ion batter-

* Corresponding author.
E-mail address: liruisz@pku.edu.cn (R. Li).
[1] These authors contributed equally to this work.

https://doi.org/10.1016/j.cclet.2024.109715
1001-8417/

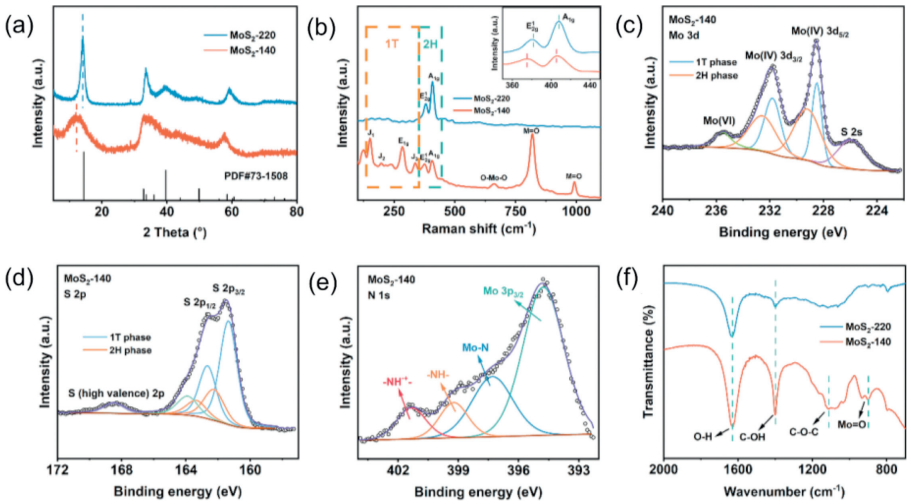

Fig. 1. Structural characterization of the as-prepared MoS_2–140 and MoS_2–220 samples. (a) XRD patterns; (b) Raman spectra; XPS spectra of (c) Mo 3d; (d) S 2p and (e) N 1s; (f) FTIR spectra.

ies [25], and Zn-ion batteries [26,27] due to its large interlayer spacing. Specifically, MoS_2 can be categorized into three phases: 1T, 2H, and 3R, with 1T and 2H phases being relatively common [28]. Different stacking orders of molybdenum and sulfur atoms determine the different properties. Typically, 1T phase MoS_2 with octahedral coordination shows metallic properties, the conductivity of which is about 10^7 higher than that of semiconductive 2H phase MoS_2 that possesses trigonal prismatic coordination and an indirect bandgap of about 1.3 eV [29,30]. The excellent conductivity of metallic 1T-phase MoS_2 endows it with great potential as a cathode material [30]. However, the thermodynamic metastability of 1T-phase MoS_2 often necessitates strategies such as heteroatom doping and guest molecule insertion, which can significantly impact the material's properties and enhance its structural stabilization [30–33].

Herein, we proposed a defect-rich MoS_2 with a substantial proportion of metallic 1T phase as the cathode of aqueous iron-ion batteries. The relatively low hydrothermal temperature enables *in-situ* O and N doping, as well as the generation of a significant amount of 1T phase and S vacancy. The presence of abundant functional groups and heteroatoms doping contributes to the stabilization of metastable 1T-phase MoS_2. As a result, the synthesized MoS_2 sample displays an impressive specific capacity of 123 mAh/g at a current density of 100 mA/g and demonstrates a stable cycling performance (88% capacity retention after 600 cycles at 200 mA/g). This work verified the feasibility of utilizing two-dimensional transition-metal dichalcogenides as a promising cathode material for high-performance aqueous iron-ion batteries.

In order to obtain different phases, the MoS_2 samples were synthesized by a facile one-pot hydrothermal approach at 140 °C and 220 °C, which were labeled as MoS_2–140 and MoS_2–220, respectively (see Experimental Section in Supporting information). Firstly, X-ray diffraction (XRD) was adopted to determine the crystal structure of the as-prepared samples. As shown in Fig. 1a, the characteristic peak of MoS_2–220 located at 14.07° corresponds to the (002) phase of hexagonal MoS_2 (PDF#73–1508) [26,34]. Compared with MoS_2–220, MoS_2–140 shows obviously weakened intensity and broadening peaks, indicating its amorphous nature which provides ample active electrochemical sites and ion diffusion routes for Fe^{2+} cations [35,36]. Moreover, the characteristic peak of the (002) phase shifts to a lower angle of 12.17° in MoS_2–140, suggesting the expansion of its layer spacing, which further decreases the diffusion energy barrier, facilitating the insertion/extraction of Fe^{2+} in the MoS_2 [26].

The Raman spectrum shown in Fig. 1b was performed to investigate the phase of as-prepared MoS_2 samples. MoS_2–220 shows two distinct peaks at 381.5 cm^{-1} and 408.1 cm^{-1}, corresponding to the in-plane E^1_{2g} vibration and out-of-plane A_{1g} vibration of 2H-phase MoS_2 [30], suggesting MoS_2–220 is composed mainly of 2H phase. Peaks representing E^1_{2g} (375.6 cm^{-1}) and A_{1g} (405.2 cm^{-1}) vibration were also observed in MoS_2–140 with reduced intensity, slight red shift, and broadening (inserted figure in Fig. 1b), suggesting weaker Mo-S bond (E^1_{2g}) and weaker interlayer interaction (A_{1g}) [35]. In addition, a reduced intensity ratio of A_{1g} and E^1_{2g} is observed in MoS_2–140, indicating an increased edge exposure that provides more active sites for Fe^{2+} ions [37]. Besides E^1_{2g} and A_{1g} peaks, the Raman spectrum of MoS_2–140 contains characteristic peaks at 150, 196, 283, and 336 cm^{-1}, corresponding to the J_1, J_2, E_{1g}, and J_3 vibration modes of 1T-phase MoS_2, respectively [38,39], indicating the coexistence of 1T and 2H phase in MoS_2–140. Concretely, E_{1g} vibration originates from the octahedral coordination of Mo atoms in 1T-phase MoS_2, while J_1, J_2, and J_3 vibration is associated with the lattice distortion occurring in the 1T phase [40]. The existence of J_1, J_2, and J_3 vibration indicates the low crystallinity of MoS_2–140, which is consistent with XRD results. Apart from the characteristic peaks related to 2H and 1T phase, three peaks located at 560.5, 817.9, and 991.3 cm^{-1} were observed. The characteristic peak at 560.5 cm^{-1} represents the vibration of O-Mo-O stretching, while peaks at 817.9 and 991.3 cm^{-1} represent the vibration of Mo=O stretching [39,41,42]. The existence of O-Mo-O and Mo=O could be attributed to the residual chemical bond in ammonium molybdate tetrahydrate that could not be broken under low hydrothermal temperature [43], leading to expanded interlayer spacing and facilitating Fe^{2+} diffusion kinetics.

X-ray photoelectron spectroscopy (XPS) was conducted to elucidate the surface chemical composition of MoS_2–140 and MoS_2–220. The full spectrum of MoS_2–140 (Fig. S1 in Supporting information) shows that the sample contains Mo, S, and O. The ratio of Mo and S elements is about 1:1.6, indicating the existence of S-vacancy defects. The high S-vacancy concentration could attribute to the excess thiourea in the hydrothermal process, which not only employed as a reductant and S source, but also adsorb on the surface of primary crystallites, hindering subsequent directional growth and forming defect-rich structure [37]. The deconvolution of Mo 3d spectrum for MoS_2–140 is shown in Fig. 1c. Peaks at 231.8 and 228.5 eV can be ascribed to Mo(IV) $3d_{3/2}$ and

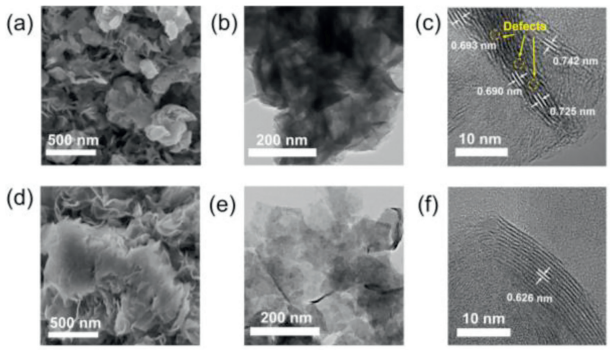

Fig. 2. (a) SEM, (b) TEM, and (c) HRTEM images of MoS_2–140 sample. (d) SEM, (e) TEM, and (f) HRTEM images of the MoS_2–220 sample.

$3d_{5/2}$ in 1T-phase MoS_2, respectively. While the peaks at 232.6 and 229.3 eV can be attributed to Mo(IV) $3d_{3/2}$ and $3d_{5/2}$ in 2H phase [44]. The difference in the binding energy between the 2H phase and 1T phase is about 0.8 eV, which is consistent with previous reports [45]. The peak at 226.0 eV can be ascribed to S 2s, and the peak at 235.5 eV could be attributed to Mo(VI) formed due to the inevitable oxidation of Mo(IV) in metastable 1T-phase MoS_2 under high-energy X-ray irradiation during the XPS testing process [27]. The deconvolution of S 2p spectrum in Fig. 1d shows similar results. The peaks at 163.4, 162.3, 162.7 and 161.4 eV can be ascribed to S $2p_{1/2}$ and S $2p_{3/2}$ in the 2H phase and 1T phase, respectively. Moreover, there are two distinct peaks observed at 163.9 and 168.5 eV, which can be attributed to the high valence S generated by oxygen incorporation [39]. However, the XPS spectra of MoS_2–220 (Figs. S2a and b in Supporting information) predominantly exhibit peaks corresponding to the 2H phase, with only a few peaks attributed to the 1T phase. The XPS spectra reveal a significant presence of the 1T phase MoS_2 in the synthesized MoS_2–140, which is consistent with the findings from Raman spectroscopy. In addition, comparing Fig. 1e and Fig. S2c (Supporting information), additional peaks at 401.4 and 399.2 eV were observed in the deconvolution of N 1s spectrum for MoS_2–140, corresponding to -$NH^{\cdot+}$- and -NH- [46,47]. This observation suggests the presence of nitrogen incorporation in MoS_2–140, which exists within the interlayer space between MoS_2 layers in the form of NH_3 or NH_4^+, stabilizing the metastable 1T phase and expanding the interlayer spacing [48].

The functional groups of the as-synthesized samples were further investigated through Fourier transform infrared spectroscopy (FTIR). As shown in Fig. 1f, the strong adsorption band at 1629 cm^{-1} that was observed in both MoS_2–140 and MoS_2–220 could be ascribed to the O–H of the adsorbed water [49]. Other adsorption bands at 1400, 1114, and 899 cm^{-1} can be attributed to C–OH, C–O-C, and Mo=O, respectively [49,50], demonstrating the presence of oxygen-containing functional groups on the MoS_2–140 surface. Although the characteristic adsorption band of N–H (1407 cm^{-1}) had not been observed in the FT-IR spectra of MoS_2–140 [43], it would be premature to dismiss the presence of N doping given that the proximity between the characteristic adsorption bands of N–H (1407 cm^{-1}) and C–OH (1400 cm^{-1}) could potentially lead to overlapping due to limited detection accuracy.

The scanning electron microscopy (SEM) and transmission electron microscopy (TEM) images of the MoS_2–140 and MoS_2–220 samples are presented in Fig. 2, revealing a lamellar structure with some agglomeration for both samples. As shown in Fig. 2c, the high-resolution transmission electron microscopy (HRTEM) reveals that the interlayer spacing of MoS_2–140 displays an average distribution around ~0.72 nm, while the interlayer spacing of MoS_2–220 is 0.626 nm (Fig. 2f), indicating the enlarged interlayer spacing expanded by O and N incorporation, which are well consistent with the XRD data. In addition, the slight difference in the observed interlayer spacing of MoS_2–140 in different places suggests the inhomogeneity of heteroatom doping. Moreover, the presence of numerous discontinuous lattice fringes observed in various positions of MoS_2–140 demonstrates its defect-rich structure (Fig. 2c and Fig. S3 in Supporting information). Energy dispersive spectroscopy (EDS) was also used to detect the distribution of elements. As shown in Fig. S4 (Supporting information), the content of O and N in MoS_2–140 is significantly higher than that in MoS_2–220, suggesting the presence of O and N doping in MoS_2–140. The element mapping of MoS_2–140 is illustrated in Fig. S5 (Supporting information), suggesting a uniform distribution of Mo, S, O, and N in the sample. The presence of abundant functional groups and heteroatoms doping confirmed by Raman, FTIR, XPS, and EDS assists in the stabilization of metastable 1T-phase MoS_2.

To investigate the electrochemical behavior of MoS_2 electrodes in aqueous iron-ion batteries, the electrochemical behaviors of Fe foil in different electrolytes were first assessed using the symmetrical Fe||Fe battery and asymmetrical Cu||Fe battery. As shown in Figs. S6 and S7 (Supporting information), the symmetrical Fe||Fe cell with 3 mol/kg (3 m) $Fe(CF_3SO_3)_2$ electrolyte exhibits superior stability (more than 1000 h) compared with 1 m $Fe(CF_3SO_3)_2$, 1 m $Fe(ClO_4)_2$, 1 m $FeSO_4$ and 1 m $FeCl_2$ electrolytes, and greatly exceeds the lifespan of the symmetrical Zn||Zn battery with 3 m $Zn(CF_3SO_3)_2$ electrolyte (less than 60 h, Fig. S7). Furthermore, no significant difference in the polarization of Fe deposition/stripping can be discerned with the 3 m $Fe(CF_3SO_3)_2$ electrolyte, verifying its stability during the cycling process. To further examine the reversibility of Fe deposition/stripping, an asymmetrical Cu||Fe battery was assembled. As shown in Fig. S8 (Supporting information), the asymmetrical Cu||Fe battery exhibits a high coulombic efficiency of ~93%, suggesting the high reversibility of the Fe deposition/stripping process.

Thus, the electrochemical properties of MoS_2–140 and MoS_2–220 were measured with 3 m $Fe(CF_3SO_3)_2$ as the electrolyte, Fe foil as the anode, and MoS_2 as the cathode (Fig. 3a). Fig. 3b compares the cyclic voltammetry (CV) curves of the MoS_2–140 and MoS_2–220 electrodes at the scan rate of 0.1 mV/s. MoS_2–140 electrode exhibits a pair of redox peaks, with the oxidation peak observed at 0.75 V (*vs.* Fe^{2+}/Fe) and the reduction peak at 0.28 V (*vs.* Fe^{2+}/Fe), while MoS_2–220 electrode demonstrates negligible current within the scanning range, indicating the exceptional electrochemical activity of MoS_2–140 in iron-ion batteries. CV curves of the MoS_2–140 electrode at different scan rates are shown in Fig. 3c. The oxidation peak (Peak 1) increases with the elevated scan rate, while the reduction peak (Peak 2) gradually diminishes at high scan rates, potentially indicating a reduced redox reversibility of the MoS_2–140 electrode under large current densities. In order to investigate the kinetic mechanism of MoS_2–140 electrode in iron-ion batteries, the relationship between the peak current (i) of Peak 1 and the scan rate (ν) was analyzed using the following Eq. 1 [51]:

$$i = a\nu^b \tag{1}$$

In Eq. 1, a and b are coefficients, with the value of b typically ranging from 0.5 to 1. A b value of 0.5 indicates the diffusion-controlled behavior in the battery, while a b value of 1 refers to a surface-controlled capacitive behavior. The value of b can be obtained by plotting $\log(i)$ against $\log(\nu)$, as shown in Fig. S9 (Supporting information). The b value for Peak 1 is 0.83, suggesting a high surface-controlled capacitive contribution. Moreover, the capacitive contribution was further quantitative studied using the following Eq. 2 proposed by Dunn [51]:

$$i = k_1\nu + k_2\nu^{1/2} \tag{2}$$

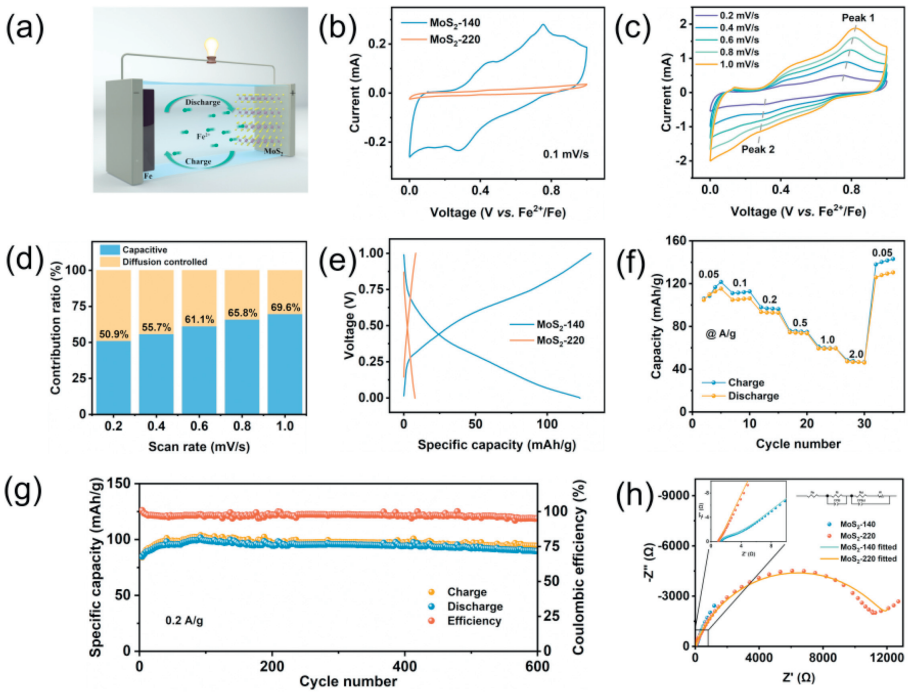

Fig. 3. (a) Schematic diagram of the battery. (b) CV curves of MoS_2–140 and MoS_2–220 electrodes at 0.1 mV/s. (c) CV curves of MoS_2–140 electrode at different scan rates. (d) Surface-controlled capacity contributions of MoS_2–140 electrode at different scan rates. (e) GCD curves of MoS_2–140 and MoS_2–220 electrodes at 100 mA/g. (f) Rate performances of MoS_2–140 electrode. (g) Long-term cycle performance of MoS_2–140 electrodes at 200 mA/g. (h) Nyquist plots of MoS_2–140 and MoS_2–220 electrodes.

where current response i at a specific voltage can be regarded as a combination of the surface-controlled *pseudo*-capacitive contribution $k_1\nu$ and diffusion-controlled contribution $k_2\nu^{1/2}$. Fig. 3d and Fig. S10 (Supporting information) show the calculated capacitive contributions are 50.9%, 55.7%, 61.1%, 65.8%, and 69.6% at scan rates of 0.2, 0.4, 0.6, 0.8, and 1.0 mV/s, respectively, revealing the high percentage of capacitive contribution. Fig. 3e displays the galvanostatic charge-discharge (GCD) curves of the MoS_2–140 and MoS_2–220 electrodes at 100 mA/g. Similar to the results obtained from the CV curves, MoS_2–140 exhibits sloping curves with small plateaus, demonstrating a remarkable discharge capacity of 123 mAh/g. In contrast, MoS_2–220 shows no discernible ability to store Fe^{2+} ions (10 mAh/g). The electrochemical properties of MoS_2 synthesized at different temperatures (100, 120, and 180 °C) were also evaluated, revealing their limited performance (Fig. S11 in Supporting information). Fig. 3f shows the rate performance of the MoS_2–140 electrode. The battery shows 121, 112, 98, 76, 61 and 48 mAh/g at current densities of 0.05, 0.1, 0.2, 0.5, 1.0 and 2.0 A/g, respectively. When the current density reverts back to 0.05 A/g, the capacity can be recovered to 143 mAh/g, indicating its good rate capability in iron-ion batteries. Power and energy densities of MoS_2–140 electrode were also calculated (Fig. S12 in Supporting information). The cycling performance of MoS_2–140 at 100 mA/g is presented in Fig. S13 (Supporting information). The initial discharge capacity is 95 mAh/g, which increases to 123 mAh/g after ~50 cycles due to the activation during the initial stage. After 200 cycles, a capacity of 115 mAh/g is obtained with a Coulombic efficiency of ~95%. When current density is increased to 200 mA/g (Fig. 3g), the MoS_2–140 electrode demonstrates a specific capacity of ~100 mAh/g and exhibits an excellent capacity retention rate of 88% after 600 cycles, indicating its outstanding cycling stability. However, the battery exhibits rapid capacity degradation as well as limited lifespan when the current density increases to 1 A/g (Fig. S14 in Supporting information), potentially attributed to the reduced reversibility of the MoS_2–140 electrode at high scan rates observed in CV curves (Fig. 3c) and the unsatisfactory cycling stability of Fe anode at large current densities (Fig. S15 in Supporting information). Considering that aqueous iron-ion batteries are primarily designed for large-scale energy storage applications, where safety, cycle life, and cost rather than power density are primary concerns, the limited performance of the MoS_2–140 electrode at large current densities can be considered acceptable.

Electrochemical impedance spectroscopy (EIS) was further conducted to investigate the kinetics in MoS_2–140 and MoS_2–220. As shown in Fig. 3h and Table S1 (Supporting information), the charge transfer resistance (R_{ct}) of MoS_2–140 ($R_{ct} = 1.596\ \Omega$) is significantly lower than that of MoS_2–220 ($R_{ct} = 12{,}789\ \Omega$), indicating the enhanced charge transfer kinetics. Furthermore, Figs. S16a and b (Supporting information) show the relationship between Z' and the reciprocal square roots of the frequency ($\omega^{-\frac{1}{2}}$) of MoS_2–140 and MoS_2–220, respectively, in which the fitted slope represents the Warburg coefficients (σ). The Fe^{2+} diffusion coefficient can be calculated using the following Eq. 3 [52]:

$$D_{Fe} = \frac{R^2T^2}{2A^2n^4F^4c^2\sigma^2} \tag{3}$$

where R, T, A, n, F, and C correspond to the gas constant, absolute temperature, electrode area, number of electrons during the redox reaction, Faraday constant, and molar concentration of Fe^{2+}, respectively. The calculated Fe^{2+} diffusion coefficient of MoS_2–140 is 1.15×10^{-12} cm^2/s, which is two orders of magnitude higher than that of MoS_2–220 (1.26×10^{-14} cm^2/s), suggesting the fast Fe^{2+} diffusion kinetics of MoS_2–140 electrode due to a large amount of conductive 1T phase as well as abundant defects.

In order to further investigate the reversible storage of Fe^{2+} in MoS_2–140 electrode, controlled experiments, inductively coupled plasma emission spectrometer (ICP), EDS, and XPS analysis were carried out. First of all, it is important to investigate the proton insertion since the acidity of aqueous $Fe(CF_3SO_3)_2$ electrolyte. Fig. S17 (Supporting information) shows cycling performances and GCD profiles of MoS_2–140 electrode in both H_2SO_4 electrolyte (pH 1) and HCl electrolyte (pH 1) at a current den-

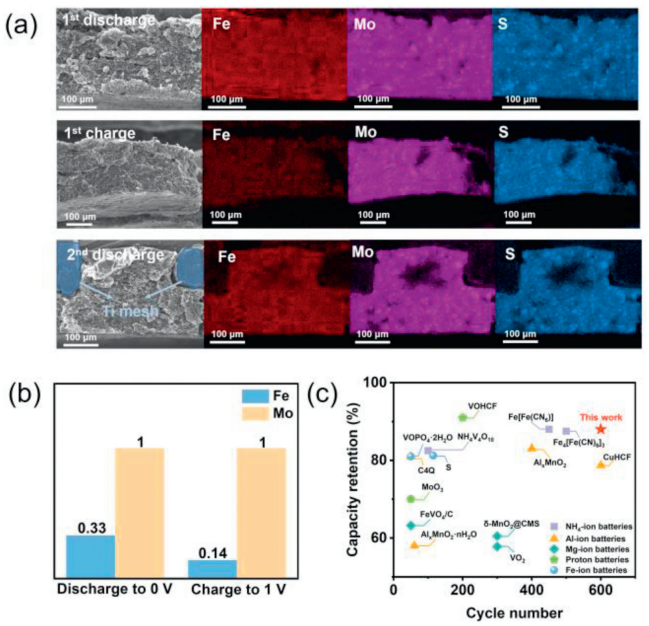

Fig. 4. (a) EDS results of the cross-section of MoS_2–140 electrodes at different SOC. (b) ICP results of MoS_2–140 electrodes at different SOC. (c) Comparison of cycling stability at low current densities of our work with other reported novel aqueous batteries [16,21,56-66].

sity of 100 mA/g, respectively, using a three-electrode system with MoS_2–140 as the working electrode, active carbon as the counter electrode and Hg/Hg_2SO_4 as the reference electrode. Different from the performance in $Fe(CF_3SO_3)_2$ electrolyte, the MoS_2–140 electrode exhibits a high initial discharge capacity of ~150 mAh/g in H_2SO_4 and HCl electrolytes, but the capacity experiences a rapid fading in the following cycles, with only 23 mAh/g after 100 cycles in H_2SO_4 electrolyte (19 mAh/g after 200 cycles in HCl electrolyte). Besides, the shape of the GCD curves of the MoS_2–140 electrode in $Fe(CF_3SO_3)_2$ and H_2SO_4/HCl electrolytes is different. Those demonstrate that proton insertion plays a significant role, but the ion storage processes are different in H_2SO_4/HCl and $Fe(CF_3SO_3)_2$ electrolytes, suggesting the Fe^{2+}/H^+ co-intercalation mechanism. EDS was performed on the cross-section of the MoS_2–140 electrode at different states of charge (SOC) (Fig. 4a and Table S2 in Supporting information). The Fe content decreases from 23.0% (first discharge) to 8.0% (first charge) and increases to 27.3% after the second discharge. The significant differences in Fe content at different SOCs prove the reversible Fe^{2+} (de)intercalation. TEM images and corresponding element mapping of MoS_2–140 electrodes at different SOCs are also displayed in Fig. S18 (Supporting information). The content of Fe decreases from 13.9 at% (discharge to 0 V) to 5.0 at% (charge to 1 V). Furthermore, the ICP of electrodes at different SOCs was also performed (Fig. 4b). The ratio of Fe:Mo increases from 0 (pristine state) to 0.33 (fully discharged state), suggesting the insertion of Fe^{2+} ions during the discharge process. When fully charged, the ratio of Fe: Mo decreases to 0.14, which is well consistent with EDS results. The reversible phase transition between the 1T and 2H phase of the MoS_2–140 electrode was also demonstrated through XPS analysis at different SOCs (Fig. S19 in Supporting information). Considering the metastable 1T-phase MoS_2 would convert to Mo(VI) under high-energy X-ray irradiation [27,35,43], only the content of the stable 2H phase was analyzed. The proportion of the 2H phase decreases from 44.7% at the charge state to 38.6% at the discharge state, demonstrating the phase transition triggered by Fe^{2+}/H^+ co-intercalation [27,40,53,54]. Comparison between our work and other state-of-the-art novel aqueous batteries, such as aqueous NH_4-ion batteries [55–57], aqueous Al-ion batteries [58–61], aqueous Mg-ion batteries [62–64], proton batteries [65,66], and aqueous Fe-ion batteries [16,20] are shown in Fig. 4c and Table S3 (Supporting information). MoS_2–140-based aqueous iron-ion battery displays remarkable cycling stability at low current densities compared with other reported novel aqueous batteries, indicating its promising application prospect in grid-scale energy storage systems.

In summary, we successfully synthesized defect-rich MoS_2 with a substantial amount of metallic 1T phase by controlling the hydrothermal temperature. Rich defects as well as abundant 1T phase contribute to the enhanced Fe^{2+} diffusion kinetics, making MoS_2–140 a promising cathode candidate for rechargeable aqueous iron-ion batteries. Notably, the electrode shows a desirable specific capacity of 123 mAh/g at 100 mA/g and a stable cycling performance with 88% capacity retention after 600 cycles at 200 mA/g. Controlled experiments combined with characterizations including EDS, ICP, and XPS elucidate the reversible Fe^{2+}/H^+ storage mechanism. This work provides a new perspective for the development of cathode materials for aqueous iron-ion batteries.

Acknowledgment

This work was supported by Shenzhen Fundamental Research Program (No. GXWD20201231165807007-20200802205241003).

Supplementary materials

Supplementary material associated with this article can be found, in the online version, at doi:10.1016/j.cclet.2024.109715.

References

[1] D. Larcher, J.M. Tarascon, Nat. Chem. 7 (2015) 19–29.
[2] P. Simon, Y. Gogotsi, Nat. Mater. 19 (2020) 1151–1163.
[3] Z. Song, G. Zhang, X. Deng, et al., Adv. Funct. Mater. 32 (2022) 2205453.
[4] Q. Li, Y. Liu, S. Guo, H. Zhou, Nano Today 16 (2017) 46–60.
[5] H. Kim, J. Hong, K.Y. Park, et al., Chem. Rev. 114 (2014) 11788–11827.
[6] D. Chao, W. Zhou, F. Xie, et al., Sci. Adv. 6 (2020) eaba4098.
[7] H. Liu, L. Jiang, B. Cao, et al., ACS Nano 16 (2022) 14539–14548.
[8] Z. Cao, H. Zhang, B. Song, et al., Adv. Funct. Mater. 33 (2023) 2300339.
[9] B. Wu, Y. Mu, Z. Li, et al., Chin. Chem. Lett. 34 (2023) 107629.
[10] J. Zhou, Q. Li, X. Hu, et al., Chin. Chem. Lett. 35 (2024) 109143.
[11] H. Liu, Z. Xin, B. Cao, et al., Adv. Funct. Mater. 34 (2024) 2309840.
[12] Z. He, F. Xiong, S. Tan, et al., Mater. Today Adv. 11 (2021) 100156.
[13] J. Liu, D. Dong, A.L. Caro, et al., ACS Central Sci 8 (2022) 729–740.
[14] A.A. Yaroshevsky, Geochem. Int. 44 (2006) 48–55.
[15] M. Chen, Q. Liu, S.W. Wang, et al., Adv. Energy Mater. 9 (2019) 1803609.
[16] Y. Xu, X. Wu, S.K. Sandstrom, et al., Adv. Mater. 33 (2021) 2105234.
[17] X. Wu, A. Markir, Y. Xu, et al., Adv. Funct. Mater. 29 (2019) 1900911.
[18] C. Li, Y. Xu, W. Deng, et al., J. Power Sources 581 (2023) 233506.
[19] C. Li, Y. Xu, W. Deng, et al., Small 20 (2024) 2305766.
[20] X. Wu, A. Markir, Y. Xu, et al., Adv. Energy Mater. 9 (2019) 1902422.
[21] C. Bai, H. Jin, Z. Gong, X. Liu, Z. Yuan, Energy Storage Mater. 28 (2020) 247–254.
[22] H. Lv, Z. Wei, C. Han, et al., Nat. Commun. 14 (2023) 3117.
[23] Y. Xu, C. Li, W. Deng, et al., Chem. Commun. 59 (2023) 8576–8579.
[24] Y. Teng, H. Zhao, Z. Zhang, et al., ACS Nano 10 (2016) 8526–8535.
[25] W. Chen, W. Wu, Z. Pan, X. Wu, H. Zhang, J. Alloy. Compd. 763 (2018) 257–266.
[26] J. Liu, P. Xu, J. Liang, et al., Chem. Eng. J. 389 (2020) 124405.
[27] S. Li, C. Huang, L. Gao, et al., Angew. Chem. Int. Ed. 61 (2022) e202211478.
[28] W.S.V. Lee, T. Xiong, X. Wang, J. Xue, Small Methods 5 (2021) 2000815.
[29] M. Acerce, D. Voiry, M. Chhowalla, Nat. Nanotechnol. 10 (2015) 313–318.
[30] Z. Lei, J. Zhan, L. Tang, Y. Zhang, Y. Wang, Adv. Energy Mater. 8 (2018) 1703482.
[31] J.R. Huang, W.X. Shi, S.Y. Xu, et al., Adv. Mater. (2023) 2306906.
[32] Y. Song, Y. Peng, S. Yao, et al., Chin. Chem. Lett. 33 (2022) 1047–1050.
[33] H.Q. Yin, L.L. Yang, H. Sun, et al., Chin. Chem. Lett. 34 (2023) 107337.
[34] J. Xie, J. Zhang, S. Li, et al., J. Am. Chem. Soc. 135 (2013) 17881–17888.
[35] S. Li, Y. Liu, X. Zhao, et al., Angew. Chem. Int. Ed. 60 (2021) 20286–20293.
[36] B. Jin, Y. Liu, J. Cui, et al., Adv. Funct. Mater. 33 (2023) 2301909.
[37] F. Zhu, H. Zhang, Z. Lu, D. Kang, L. Han, J. Energy Storage 42 (2021) 103046.
[38] S. Shi, Z. Sun, Y.H. Hu, J. Mater. Chem. A 6 (2018) 23932–23977.
[39] D. Tang, J. Li, Z. Yang, et al., Chem. Eng. J. 428 (2022) 130954.
[40] F. Shao, Y. Huang, X. Wang, et al., Chem. Eng. J. 448 (2022) 137688.
[41] S. Bai, C. Chen, M. Cui, et al., RSC Adv 5 (2015) 50783–50789.
[42] F. Zeng, M. Yu, W. Cheng, et al., Small 16 (2020) 2001905.
[43] H. Liang, Z. Cao, F. Ming, et al., Nano Lett. 19 (2019) 3199–3206.

[44] J. Sun, Z. Zhang, G. Lian, et al., ACS Nano 16 (2022) 12425–12436.
[45] J. Liu, N. Gong, W. Peng, et al., Chem. Eng. J. 428 (2022) 130981.
[46] M. Huang, Y. Mai, L. Zhao, et al., Electrochim. Acta 388 (2021) 138624.
[47] L. Xiang, C.G. Niu, N. Tang, et al., Chem. Eng. J. 408 (2021) 127281.
[48] Q. Liu, X. Li, Q. He, et al., Small 11 (2015) 5556–5564.
[49] S. Tian, X. Zhang, Z. Zhang, Chem. Eng. J. 409 (2021) 128200.
[50] S. Kumari, K. Singh, P. Singh, S. Kumar, A. Thakur, SN Appl. Sci. 2 (2020) 1439.
[51] T. He, X. Kang, F. Wang, et al., Mater. Sci. Eng. R 154 (2023) 100737.
[52] Z. Yao, W. Zhang, X. Ren, et al., ACS Nano 16 (2022) 12095–12106.
[53] Z. Lin, Y. Liu, U. Halim, et al., Nature 562 (2018) 254–258.
[54] M. Huang, Y. Mai, G. Fan, et al., J. Alloy. Compd. 871 (2021) 159541.
[55] X. Wu, Y. Xu, H. Jiang, et al., ACS Appl. Energ. Mater. 1 (2018) 3077–3083.
[56] H. Li, J. Yang, J. Cheng, T. He, B. Wang, Nano Energy 68 (2020) 104369.
[57] M. Xia, X. Zhang, H. Yu, et al., Chem. Eng. J. 421 (2021) 127759.
[58] C. Wu, S. Gu, Q. Zhang, et al., Nat. Commun. 10 (2019) 73.
[59] Y. Li, L. Liu, Y. Lu, et al., Adv. Funct. Mater. 31 (2021) 2102063.
[60] Q. Ran, H. Shi, H. Meng, et al., Nat. Commun. 13 (2022) 576.
[61] Q. Hao, F. Chen, X. Chen, et al., ACS Appl. Mater. Interfaces 15 (2023) 34303–34310.
[62] H. Zhang, K. Ye, K. Zhu, et al., Chem. Eur. J. 23 (2017) 17118–17126.
[63] H. Zhang, D. Cao, X. Bai, J. Power Sources 444 (2019) 227299.
[64] X. Bai, D. Cao, Z. Jiang, H. Zhang, Inorg. Chem. Front. 9 (2022) 485–493.
[65] A. Ikezawa, Y. Koyama, T. Nishizawa, H. Arai, J. Mater. Chem. A 11 (2023) 2360–2366.
[66] J. Yang, W. Hou, L. Ye, et al., Small 20 (2024) 2305386.